

# Evolution of Iodoplumbate Complexes in Methylammonium Lead Iodide Perovskite Precursor Solutions

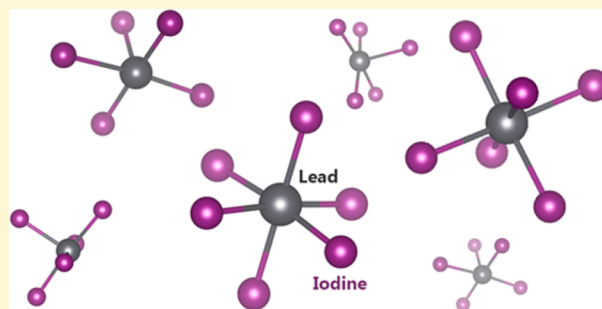
Alexander Sharenko,<sup>†</sup> Cameron Mackeen,<sup>‡</sup> Leila Jewell,<sup>‡</sup> Frank Bridges,<sup>‡</sup> and Michael F. Toney<sup>\*,†</sup>

<sup>†</sup>Stanford Synchrotron Radiation Lightsource, SLAC National Accelerator Laboratory, Menlo Park, California 94025, United States

<sup>‡</sup>Department of Physics, University of California at Santa Cruz, 1156 High Street, Santa Cruz, California 95064, United States

**S** Supporting Information

**ABSTRACT:** Here we investigate the local structure present in single-step precursor solutions of methylammonium lead iodide (MAPbI<sub>3</sub>) perovskite as a function of organic and inorganic precursor ratio, as well as with hydriodic acid (HI), using X-ray absorption spectroscopy. An excess of organic precursor as well as the use of HI as a processing additive has been shown to lead to the formation of smooth, continuous, pinhole free MAPbI<sub>3</sub> films, whereas films produced from precursor solutions containing molar equivalents of methylammonium iodide (MAI) and PbI<sub>2</sub> lead to the formation of a discontinuous, needlelike morphology. We now show that as the amount of excess MAI in the precursor solution is increased, the iodide coordination of iodoplumbate complexes present in solution increases. The use of HI results in a similar increase in iodide coordination. We therefore offer insight into how solution chemistry can be used to control MAPbI<sub>3</sub> thin film morphology by revealing a strong correlation between the lead coordination chemistry in precursor solutions and the surface coverage and morphology of the resulting MAPbI<sub>3</sub> film.



## 1. INTRODUCTION

Lead halide perovskites have attracted an immense amount of attention over the past several years because of the rapid ascent of their photovoltaic efficiency.<sup>1,2</sup> To date, solution-processed lead halide perovskite photovoltaic devices have been reported with certified power conversion efficiencies exceeding 20%.<sup>3</sup> Recent advances are in large part due to the development of processing techniques that produce smooth, continuous films necessary for the active layer in a high-efficiency photovoltaic device. Forming such a smooth, continuous film using a single-step solution processing protocol requires careful control of the chemistry of precursor solutions and/or the film deposition conditions.<sup>4,5</sup> Specifically, it is known that spin-casting a solution containing molar equivalents of methylammonium iodide (MAI) and PbI<sub>2</sub> fails to produce a continuous film and instead produces a discontinuous, needlelike morphology that produces shorts and a relatively low power conversion efficiency upon incorporation into a photovoltaic device. A common workaround is to cast films from solutions containing a molar excess of MAI, which produces a more continuous, smoother MAPbI<sub>3</sub> film.<sup>6,7</sup> A disadvantage of this methodology is that the excess MAI must then be removed from the film via thermal decomposition, requiring higher temperature and/or longer annealing protocols that can lead to grain coarsening and film roughening.<sup>8</sup> An alternative method for producing smooth, continuous lead halide perovskite films with a single-step protocol is to incorporate a small amount of hydriodic acid (HI) into the casting solution.<sup>9</sup> HI has therefore been used as

an additive for the fabrication of high-efficiency photovoltaic devices.<sup>10–12</sup>

Lead halide perovskite precursor solutions containing both the inorganic and organic precursor have been described as soft coordination networks<sup>7</sup> or sol-gels.<sup>13</sup> Stampelcoskie et al. suggested that PbI<sub>2</sub> and the higher-order iodoplumbate coordination complexes PbI<sub>3</sub><sup>−</sup> and PbI<sub>4</sub><sup>2−</sup> exist in equilibrium in solutions where the iodide concentration exceeds the lead concentration by more than an order of magnitude.<sup>14</sup> Changes in the absorption band edge of precursor solutions as a function of precursor molar ratio have thus been qualitatively explained in terms of relative changes in the populations of iodoplumbate coordination complexes that are present in solution.<sup>7</sup> The presence of these complexes in perovskite precursor solutions and their exact structure and relationship to specific precursor chemistries, however, have not been directly verified or quantified and been only indirectly inferred, nor, to the best of our knowledge, has any experimental evidence been presented to explain what role HI serves in precursor solutions. Herein, we use X-ray absorption spectroscopy of the Pb L-III edge to probe the local structure of the Pb ions in precursor solutions as a function of the precursor molar ratio and the presence of HI to aid in the development of a mechanistic understanding of how solution chemistry can be tuned to

Received: November 21, 2016

Revised: January 24, 2017

Published: February 2, 2017

produce the smooth, continuous films required for the fabrication of efficient photovoltaic devices.

Extended X-ray absorption fine structure (EXAFS) refers to the oscillatory region of an X-ray absorption spectrum beginning  $\sim 30$  eV above an absorption edge. This oscillatory structure, denoted as  $\chi$ , arises from the backscattering of photoelectrons from various shells of neighboring atoms and can be expressed in terms of total absorption  $\mu$  for the edge of interest and average absorption above the edge  $\mu_0$ :

$$\chi(E) = \frac{\mu(E) - \mu_0(E)}{\mu_0(E)} \quad (1)$$

The extracted  $\chi(E)$  data are then converted from energy to wave vector or  $k$ -space. From perturbation theory,  $\chi(k)$  is a sum of waves of the following form:<sup>15</sup>

$$k\chi(k) = \sum_i \frac{N_i S_o^2 F(k, r_i) e^{-2\sigma_i^2 k^2}}{r_i^2} \sin[2kr_i + \phi_i(k, r_i)] \quad (2)$$

where  $k$  is the photoelectron wave vector,  $N$  is the number of neighbors (coordination number),  $S_o^2$  is the amplitude reduction factor (equal to 1.0 here),  $F(k, r)$  is the backscattering amplitude,  $\phi(k, r)$  is the backscattering phase, and  $\sigma$  is the width of the pair distribution function. Waves at different  $r$  add constructively or destructively, leading to a complex function in  $k$ -space. A Fourier transform (FT) of  $k\chi(k)$  into real space ( $r$ -space) then produces peaks corresponding to the distances from the absorbing atom to different neighbor atoms. The phase term  $\phi(k, r)$  can be approximately written as  $-2k\alpha + \varphi(k)$ ; when combined with the  $2kr$  term, the effective distance on an EXAFS plot is  $r - \alpha$ , where  $\alpha$  is the phase shift of approximately 0.3–0.5 Å. As a consequence of the phase shift, the peaks on an EXAFS plot are therefore shifted to shorter distances compared to actual atomic spacings. By fitting the data using eq 2 (the EXAFS equation), local structure information about the absorbing atom can be extracted up to approximately 4–5 Å, including the distance to neighboring (backscattering) atoms, their chemical identity, and the coordination number.<sup>16</sup> In this study, MAPbI<sub>3</sub> precursor solutions in dimethylformamide (DMF) with different PbI<sub>2</sub>:MAI molar ratios (1:1, 1:1.5, and 1:3) as well as 1:1 PbI<sub>2</sub>/MAI precursor solutions with different amounts of HI and a solution of PbI<sub>2</sub> without MAI are investigated via EXAFS. Data were acquired at approximately 5 K using a helium cryostat on solutions that were flash-frozen in liquid nitrogen to prevent hydrogen gas evolution during X-ray irradiation, which complicates data collection and can introduce measurement artifacts.<sup>17</sup> Additionally, sample cooling is recommended for samples containing soft metals to prevent EXAFS signal attenuation due to thermal effects.<sup>18</sup> Sample cooling thus leads to higher EXAFS amplitudes at high wave vectors and hence facilitates the interpretation of EXAFS. Further details about sample preparation as well as data collection and reduction are provided in the [Supporting Information](#).

## 2. RESULTS AND DISCUSSION

The data were fit in  $r$ -space using a sum of theoretical pair functions calculated from a PbI<sub>2</sub>–DMF crystal structure<sup>19</sup> using FEFF7.<sup>20</sup> These pair functions [Pb–O, Pb–I(1), Pb–I(2), and Pb–I(3)] are based on the atomic spacings within the crystal structure, which serve as starting points for the fits. For each pair, the distribution of distances is a Gaussian of width  $\sigma$  and

amplitude  $N$ . The disorder for various shells of atoms is inferred from  $\sigma^2$ , the correlated Debye–Waller factor, with disorder increasing with the value of  $\sigma^2$ . The left side of [Figure 1](#) displays the  $r$ -space EXAFS data of each sample and the fit,

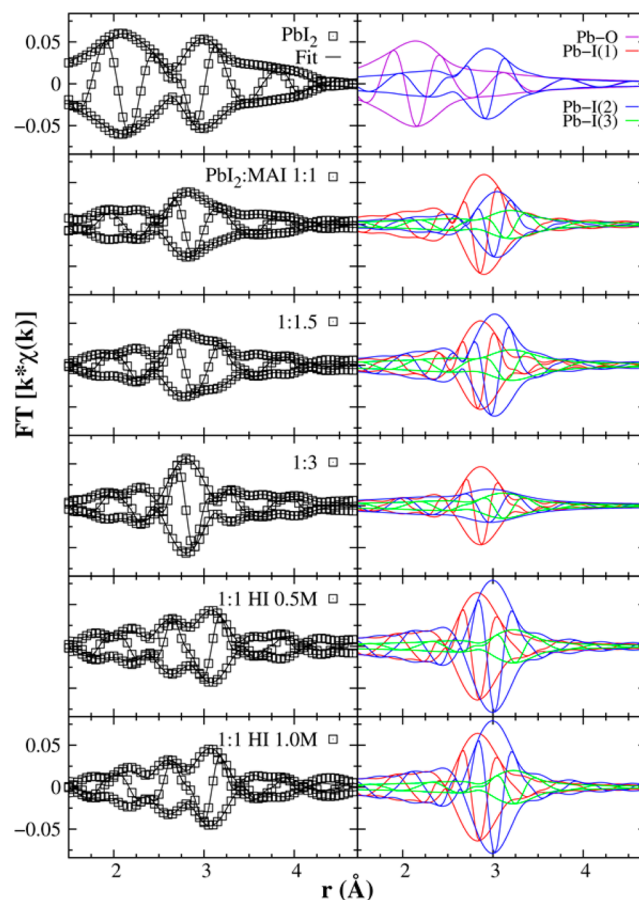


**Figure 1.** Fourier transform of eq 2 (i.e., EXAFS equation), FT [ $k\chi(k)$ ], vs  $r$ -space distance from the absorbing Pb atom ( $r$ ). Both the magnitude (outer envelope) and the real part (inner curves) of the Fourier transform are shown for the data. The left column shows the extended X-ray absorption fine structure (EXAFS)  $r$ -space data ( $\square$ ) for six frozen single-step MAPbI<sub>3</sub> precursor solutions with corresponding fits (—): PbI<sub>2</sub>, 1:1 PbI<sub>2</sub>:MAI, 1:1.5 PbI<sub>2</sub>:MAI, 1:3 PbI<sub>2</sub>:MAI, 1:1 PbI<sub>2</sub>:MAI with 0.5 M HI, and 1:1 PbI<sub>2</sub>:MAI with 1.0 M HI (from top to bottom, respectively). The right column shows the individual components used in the fits for each sample.

while the right side displays the individual Pb–I and/or Pb–O components. The PbI<sub>2</sub> plot is distinctly different from the rest of the data in that it exhibits a large peak at approximately 2.2 Å. This peak corresponds to a Pb–O bond, consistent with the knowledge that DMF coordinates with Pb<sup>2+</sup> ions in solution via the formation of Pb–O bonds.<sup>21</sup> The PbI<sub>2</sub> data additionally exhibit a large, broad peak at approximately 3 Å that we have fit using a single Pb–I component.

In contrast, the data from solutions containing PbI<sub>2</sub> and MAI required three Pb–I components to adequately fit the data (for further discussion of the components used for the fits, see the [Supporting Information](#)). As illustrated in [Figure 2](#), the first two Pb–I components for the samples with HI are very well ordered with small  $\sigma^2$  values. They dominate the  $r$ -space data, and the interference between these two components produces the dip at 2.85 Å that is not observed in the other samples.

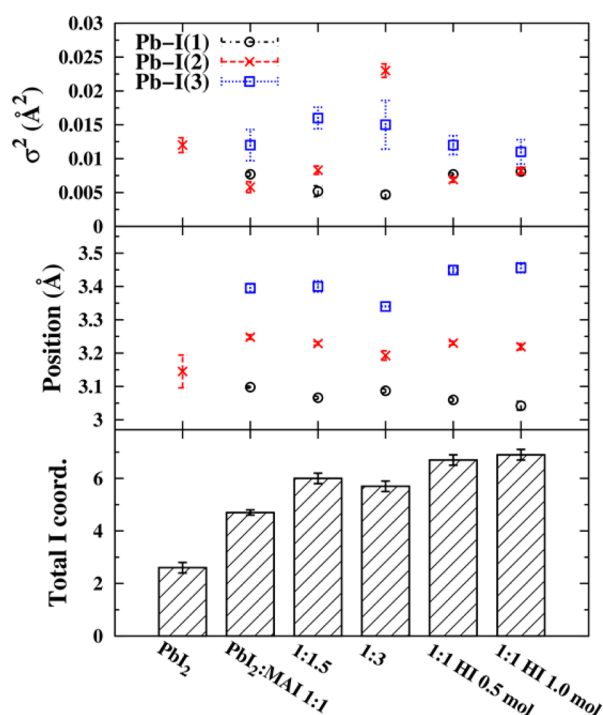


**Figure 2.** Real-space extended X-ray absorption fine structure (EXAFS) fit parameters extracted from Figure 1. The top panel plots the correlated Debye–Waller factor ( $\sigma^2$ ), the middle panel the Pb–I components’ positions from the absorbing Pb atom, and the bottom panel the total iodide coordination number of the Pb atoms in solution. Note that disorder increases as the value of  $\sigma^2$  increases and the Pb atoms in both  $\text{PbI}_2$  and  $\text{MAPbI}_3$  exhibit octahedral iodide coordination ( $\text{PbI}_6$ ). For detailed values, see Table S1.

These samples’ Pb–I(3) component, however, is slightly broader and less well-defined. For the samples without HI, the Pb–I(2) and Pb–I(3) components generally become increasingly disordered as the concentration of MAI increases from 1 to 3 M, with the Pb–I(2) component of the 1:3  $\text{PbI}_2/\text{MAI}$  sample exhibiting significantly more disorder than any component in any of the samples.

Given the 10–15% systemic error for coordination numbers from EXAFS fits as a result of correlations between  $N$  and  $\sigma$ ,<sup>15</sup> Pb ions’ total iodide coordination generally increases with an increase in MAI concentration and with the use of HI. Specifically, the total iodide coordination number increases from the  $\text{PbI}_2$  (no MAI) sample to the 1:1  $\text{PbI}_2/\text{MAI}$  sample and then again to the 1:1.5  $\text{PbI}_2/\text{MAI}$  sample. The coordination number then remains constant within experimental error for the 1:1.5 and 1:3  $\text{PbI}_2/\text{MAI}$  samples. The iodide coordination number is largest, however, for the samples incorporating HI. The use of HI thus increases iodide coordination without introducing significantly more structural disorder in contrast to the use of excess MAI that increases both coordination number and structural disorder.

In general, the measured Pb–I( $n$ ) distances group into three rather distinct spacings:  $\sim 3.1$ ,  $\sim 3.2$ – $3.25$ , and  $\sim 3.4$  Å (middle panel of Figure 2 and Table S1). Some insight into the possible origin of these spacings can be obtained by reference to the Pb–I bond lengths in  $\text{PbI}_2$ –DMF crystalline complexes<sup>19,22,23</sup> where extended octahedral Pb–I fragments are observed. These complexes’ structures have been determined with X-ray diffraction to understand their function as intermediate phases in the fabrication of  $\text{MAPbI}_3$  films.<sup>22,23</sup> Our data are similar to

data for these complexes in that both sets of data can be grouped into three distinct spacing regimes with comparable distances (Figure S2). This is in contrast to the Pb–I bond lengths in  $\text{PbI}_2$ , which has only a single spacing, and tetragonal  $\text{MAPbI}_3$ , which has three spacings but lacks a spacing comparable to the Pb–I(3) spacing measured for our data. On the basis of these comparisons, we speculate that the iodoplumbate complexes that we observe in the perovskite precursor solutions are most similar to the extended octahedral Pb–I fragments in previously reported  $\text{PbI}_2$ –DMF crystalline compounds rather than to  $\text{PbI}_2$  or  $\text{MAPbI}_3$ , albeit with longer terminal Pb–I bonds. Furthermore, the samples with HI exhibit nearly identical pair distances for each Pb–I component. Their Pb–I(1) component is slightly shorter and their Pb–I(3) component slightly longer compared to those of the samples without HI, suggesting the use of HI leads to a slightly different complex compared to the use of excess MAI. There is also likely a very small Pb–O contribution for the 1:1  $\text{PbI}_2/\text{MAI}$  sample near 2 Å, but multishell fits including a Pb–O component are not significant using the Hamilton F-test (discussed further below).<sup>24</sup>

We now present the X-ray absorption near edge structure (XANES) data of the measured samples (Figure 3). As XANES

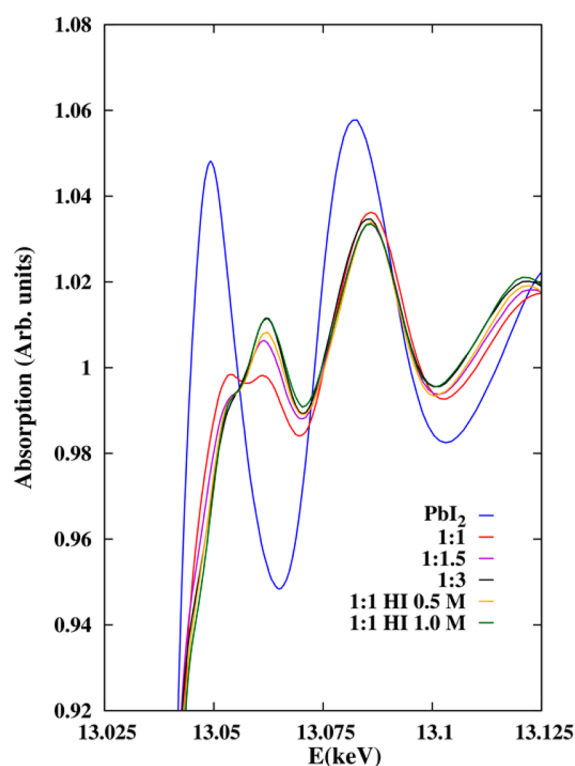


**Figure 3.** Pb L-III edge X-ray absorption near edge structure (XANES) spectra of the measured samples. The legend refers to the  $\text{PbI}_2/\text{MAI}$  molar ratio with the “ $\text{PbI}_2$ ” sample not containing any MAI.

is a probe of the local chemical bonding environment of an absorbing atom, it can be used to provide further structural insight complementary to EXAFS. The  $\text{PbI}_2$  XANES data exhibit large peaks at 13050 and 13082 eV. The samples containing both  $\text{PbI}_2$  and MAI exhibit significantly less intense peaks at approximately 13061 and 13085 eV similar to simulated XANES spectra of higher-order iodoplumbate complexes.<sup>25</sup> The 1:1  $\text{PbI}_2/\text{MAI}$  data are unique in that its



peak at 13061 eV is noticeably less intense than the spectra from the other samples containing both  $\text{PbI}_2$  and MAI, and it exhibits a large shoulder at approximately 13052 eV not present in any of the other spectra.

The XANES data additionally exhibit an isosbestic point at approximately 13056 eV. As the higher-order iodoplumbate complexes exhibit extremely similar XANES spectra that greatly differ from the XANES spectrum of  $\text{PbI}_2$ ,<sup>25</sup> and as X-ray spectroscopy data are a weighted average of the coordination environment of all absorbing atoms in solution, the presence of an isosbestic point is consistent with spectra with contributions from both Pb ions with  $\text{PbI}_2$ -like coordination and Pb ions present in higher-order iodoplumbate complexes, the relative proportion of each shifting as a function of the relative MAI or HI concentration. We have exploited this observation to improve our understanding of the unique XANES spectra of the 1:1  $\text{PbI}_2$ /MAI sample by performing a linear combination fit of its real-space EXAFS spectra using the  $\text{PbI}_2$  and 1:3  $\text{PbI}_2$ /MAI samples as standards (Figure S3). The 1:1  $\text{PbI}_2$ /MAI EXAFS data can be modeled using approximately 22%  $\text{PbI}_2$  and 78% 1:3  $\text{PbI}_2$ /MAI. When we then use these same weightings in corresponding sums of the XANES data to reconstruct the 1:1  $\text{PbI}_2$ /MAI XANES data, we find this reconstruction matches the 1:1  $\text{PbI}_2$ /MAI XANES data extremely well (Figure 4). This linear combination fitting then suggests that the local

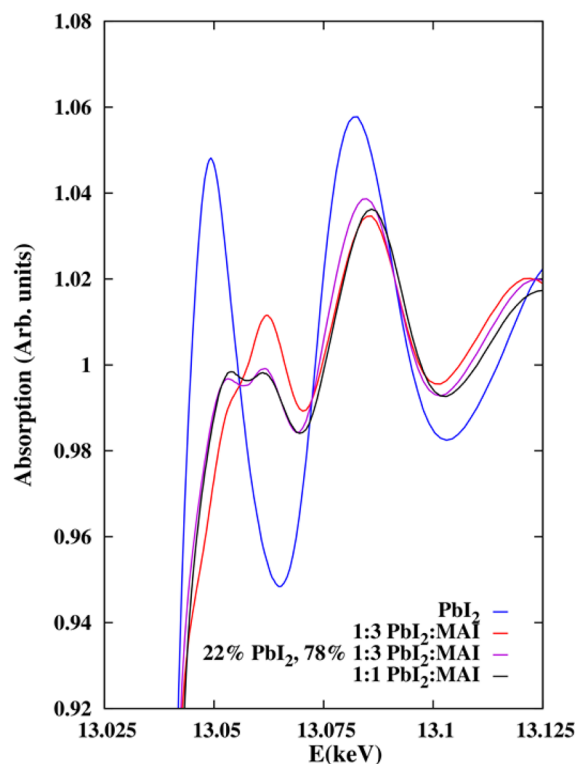


**Figure 4.** Linear combination fit of the 1:1  $\text{PbI}_2$ /MAI X-ray absorption near edge structure (XANES) data.

chemical bonding environment of the 1:1  $\text{PbI}_2$ /MAI sample likely does have a small Pb–O component similar to that of the  $\text{PbI}_2$  sample. This similarity is likely due to the presence of some remaining  $\text{PbI}_2$ –DMF coordination in the 1:1  $\text{PbI}_2$ /MAI sample. The difficulty in obtaining a fit with a Pb–O component included for the 1:1  $\text{PbI}_2$ /MAI EXAFS data arises because the Pb–O peak in this sample is small and does not

significantly contribute to its overall amplitude; therefore, the quality of the fit only slightly decreases when this peak is removed. In the simpler, two-component linear combination fit, the ratio of Pb–O to Pb–I is fixed in the  $\text{PbI}_2$  data, and the fit is slightly better in the 1:1  $\text{PbI}_2$ /MAI linear combination data near 2 Å (Figure S3) compared to the EXAFS data fit using the theoretical pair functions (Figure 1). The very good fit of the reconstructed XANES data relative to the experimental XANES data using the weighting from the EXAFS linear combination fitting therefore indicates that a small amount of Pb–O coordination is present in the 1:1 sample but not for higher concentrations of MAI.

The presented EXAFS data then reveal that DMF coordinates to  $\text{PbI}_2$  through the formation of Pb–O bonds but that as MAI is added to the solution,  $\text{I}^-$  ions displace DMF molecules to form higher-order iodoplumbate complexes. In general, the total iodide coordination number and structural disorder of these complexes increase with an increase in MAI concentration. The presented XANES data and the associated linear combination fitting additionally suggest that excess MAI or HI must be added to solutions to fully displace coordinated DMF molecules as the 1:1  $\text{PbI}_2$ /MAI XANES data could be reconstructed with a significant contribution from the  $\text{PbI}_2$  XANES data, which EXAFS revealed to encompass significant Pb–DMF coordination. EXAFS data also revealed that the use of HI both increases the total iodide coordination number with little decrease in structural order and slightly alters the structure of iodoplumbate complexes in solution by shortening the Pb–I(1) component and expanding the Pb–I(3) component compared to those seen with the use of a molar excess of MAI. The complexes formed via the use of HI exhibited higher iodide coordination numbers compared to the use of equivalent concentrations of MAI, which may just be the result of the more efficient and complete dissociation of HI compared to that of MAI, thus resulting in a higher concentration of  $\text{I}^-$  ions at similar HI and MAI concentrations. On the basis of comparisons of Pb–I spacings, it appears the iodoplumbate complexes present in single-step  $\text{MAPbI}_3$  precursor solutions are most similar to known isolated intermediate phases produced during the synthesis of  $\text{MAPbI}_3$  rather than to  $\text{PbI}_2$  or  $\text{MAPbI}_3$ , but in the case of the solutions containing HI or excess MAI without coordinated solvent molecules.

Having identified the presence of higher-order iodoplumbate complexes in  $\text{MAPbI}_3$  precursor solutions as the result of the use of excess MAI or HI, we are able to offer some mechanistic insight into how these processing conditions may affect film formation. The presence of coordinated solvent in 1:1  $\text{PbI}_2$ /MAI solutions likely leads to the needlelike, discontinuous film morphology these films produce as this morphology is similar to that of the  $\text{PbI}_2$ –DMF crystals precipitated from supersaturated  $\text{PbI}_2$ /MAI solutions.<sup>13</sup> The improved morphology associated with use of excess MAI or HI is thus likely in part the result of the elimination of  $\text{PbI}_2$ –DMF coordination. Additionally, the higher-order iodoplumbate complexes these conditions generate in solution have been shown to be important to proposed solid state transformation pathways associated with smooth, continuous perovskite films.<sup>23,26</sup> The increased solubility associated with higher-order iodoplumbate complexes will also change the kinetics of film formation during deposition, which has proven to be a generally useful strategy for fabricating smooth, continuous perovskite films.<sup>27–29</sup> The specific chemical complexes present in solution also directly affect the progression of phases precipitated from solution as

described by Ostwald's Rule of Stages.<sup>30</sup> However, because of the limitations of our data, specifically the low signal-to-noise ratio and overlapping multiple scattering features at larger real spacings, we cannot comment on various hypotheses about the role nanoparticles present in solution may play in film formation.<sup>7,31</sup> Interestingly, the slightly altered iodoplumbate structure generated in solution as a result of the use of HI compared to excess MAI may in part explain recent observations that HI stabilizes the cubic polymorph of MAPbI<sub>3</sub> at room temperature.<sup>32</sup>

### 3. CONCLUSIONS

In summary, we have used Pb L-III edge EXAFS and XANES data of single-step MAPbI<sub>3</sub> precursor solutions to reveal the lead coordination environment as a function of precursor solution chemistry. It was found that as excess MAI is added to solutions I<sup>−</sup> ions displace coordinated DMF molecules to form higher-order iodoplumbate complexes, i.e., PbI<sub>4</sub><sup>2−</sup>, PbI<sub>5</sub><sup>3−</sup>, and PbI<sub>6</sub><sup>4−</sup>. Solutions containing molar equivalents of PbI<sub>2</sub> and MAI exhibited significant DMF coordination, perhaps explaining the extremely discontinuous, needlelike film morphology these films produce. When PbI<sub>2</sub> and MAI are combined in DMF, the iodoplumbate complexes that form most closely resemble the solid state intermediate complexes identified as being mechanistically important for the synthesis of MAPbI<sub>3</sub>, rather than PbI<sub>2</sub> or MAPbI<sub>3</sub> itself, albeit without coordinated solvent in the case of solutions with HI or excess MAI. Importantly, we have offered what to the best of our knowledge is the first experimental evidence of the role HI plays as a solvent additive in improving MAPbI<sub>3</sub> film morphology. HI acts as a source of I<sup>−</sup> ions, thus allowing the formation of the iodoplumbate complexes formed with the addition of excess MAI, but with a slightly increased coordination number, slightly less structural disorder, and a modified structure. These results may more generally explain the usefulness of other halogen-containing solution additives as means of improving film morphology.<sup>33–35</sup> Our results offer important information about the coordination chemistry and local structural environment of single-step perovskite precursor solutions, which furthers our mechanistic understanding of how solution chemistry can be used to tune final film morphology by carefully controlling the lead coordination complexes present in solution. Such understanding will become increasingly important as perovskite chemistries become more diverse<sup>12,36</sup> and more robust, scalable solution-processing protocols are developed for the manufacture of large area perovskite devices and modules.<sup>37,38</sup>

### ■ ASSOCIATED CONTENT

#### Supporting Information

The Supporting Information is available free of charge on the ACS Publications website at DOI: 10.1021/acs.chemmater.6b04917.

Sample preparation, data acquisition, and fitting details (PDF)

### ■ AUTHOR INFORMATION

#### Corresponding Author

\*E-mail: mftoney@slac.stanford.edu.

#### ORCID

Alexander Sharenko: 0000-0003-2838-0255

### Notes

The authors declare no competing financial interest.

### ■ ACKNOWLEDGMENTS

This work was supported by the Laboratory Directed Research and Development Program at SLAC under Contract DE-AC02-76-SF00515. Use of the Stanford Synchrotron Radiation Lightsource, SLAC National Accelerator Laboratory, is supported by the U.S. Department of Energy, Office of Science, Office of Basic Energy Sciences, under Contract DE-AC02-76-SF00515. The authors thank Drs. Sharon Bone and Ryan Davis for their help with data interpretation and acquisition, respectively. Additionally, Kevin A. Bush is thanked for his invaluable assistance with sample preparation and Dr. Matt Newville for his assistance with proof of concept data acquisition.

### ■ REFERENCES

- (1) Park, N.-G. Perovskite Solar Cells: An Emerging Photovoltaic Technology. *Mater. Today* **2015**, *18* (2), 65–72.
- (2) Berry, J.; Buonassisi, T.; Egger, D. A.; Hodes, G.; Kronik, L.; Loo, Y.-L.; Lubomirsky, I.; Marder, S. R.; Mastai, Y.; Miller, J. S.; et al. Hybrid Organic–Inorganic Perovskites (HOIPs): Opportunities and Challenges. *Adv. Mater.* **2015**, *27*, 5102–5112.
- (3) National Renewable Energy Laboratory Efficiency Chart. [http://www.nrel.gov/ncpv/images/efficiency\\_chart.jpg](http://www.nrel.gov/ncpv/images/efficiency_chart.jpg) (accessed October 13, 2016).
- (4) Stranks, S. D.; Nayak, P. K.; Zhang, W.; Stergiopoulos, T.; Snaith, H. J. Formation of Thin Films of Organic–Inorganic Perovskites for High-Efficiency Solar Cells. *Angew. Chem., Int. Ed.* **2015**, *54* (11), 3240–3248.
- (5) Sharenko, A.; Toney, M. F. Relationships between Lead Halide Perovskite Thin-Film Fabrication, Morphology, and Performance in Solar Cells. *J. Am. Chem. Soc.* **2016**, *138* (2), 463–470.
- (6) Wang, Q.; Shao, Y.; Dong, Q.; Xiao, Z.; Yuan, Y.; Huang, J. Large Fill-Factor Bilayer Iodine Perovskite Solar Cells Fabricated by a Low-Temperature Solution-Process. *Energy Environ. Sci.* **2014**, *7* (7), 2359–2365.
- (7) Yan, K.; Long, M.; Zhang, T.; Wei, Z.; Chen, H.; Yang, S.; Xu, J. Hybrid Halide Perovskite Solar Cell Precursors: The Colloidal Chemistry and Coordination Engineering behind Device Processing for High Efficiency. *J. Am. Chem. Soc.* **2015**, *137* (13), 4460–4468.
- (8) Zhang, W.; Saliba, M.; Moore, D. T.; Pathak, S. K.; Hörantner, M. T.; Stergiopoulos, T.; Stranks, S. D.; Eperon, G. E.; Alexander-Webber, J. A.; Abate, A. Ultrasoft Organic–inorganic Perovskite Thin-Film Formation and Crystallization for Efficient Planar Heterojunction Solar Cells. *Nat. Commun.* **2015**, *6*, 6142.
- (9) Eperon, G. E.; Stranks, S. D.; Menelaou, C.; Johnston, M. B.; Herz, L. M.; Snaith, H. J. Formamidinium Lead Trihalide: A Broadly Tunable Perovskite for Efficient Planar Heterojunction Solar Cells. *Energy Environ. Sci.* **2014**, *7* (3), 982–988.
- (10) Heo, J. H.; Song, D. H.; Han, H. J.; Kim, S. Y.; Kim, J. H.; Kim, D.; Shin, H. W.; Ahn, T. K.; Wolf, C.; Lee, T.-W.; et al. Planar CH<sub>3</sub>NH<sub>3</sub>PbI<sub>3</sub> Perovskite Solar Cells with Constant 17.2% Average Power Conversion Efficiency Irrespective of the Scan Rate. *Adv. Mater.* **2015**, *27*, 3424–3430.
- (11) Im, S. H.; Heo, J.-H.; Han, H. J.; Kim, D.; Ahn, T. 18.1% Hysteresis-Less Inverted CH<sub>3</sub>NH<sub>3</sub>PbI<sub>3</sub> Planar Perovskite Hybrid Solar Cells. *Energy Environ. Sci.* **2015**, *8*, 1602–1608.
- (12) McMeekin, D. P.; Sadoughi, G.; Rehman, W.; Eperon, G. E.; Saliba, M.; Hörantner, M. T.; Haghighirad, A.; Sakai, N.; Korte, L.; Rech, B.; et al. A Mixed-Cation Lead Mixed-Halide Perovskite Absorber for Tandem Solar Cells. *Science* **2016**, *351* (6269), 151–155.
- (13) Kerner, R. A.; Zhao, L.; Xiao, Z.; Rand, B. P. Ultrasoft Metal Halide Perovskite Thin Films via Sol–gel Processing. *J. Mater. Chem. A* **2016**, *4* (21), 8308–8315.

- (14) Stampelcoskie, K. G.; Manser, J. S.; Kamat, P. V. Dual Nature of the Excited State in Organic–inorganic Lead Halide Perovskites. *Energy Environ. Sci.* **2015**, *8* (1), 208–215.
- (15) Teo, B.-K. *EXAFS: Basic Principles and Data Analysis*; Springer: Dordrecht, The Netherlands, 1986.
- (16) Rehr, J. J.; Albers, R. C. Theoretical Approaches to X-Ray Absorption Fine Structure. *Rev. Mod. Phys.* **2000**, *72* (3), 621–654.
- (17) Meents, A.; Gutmann, S.; Wagner, A.; Schulze-Briesse, C. Origin and Temperature Dependence of Radiation Damage in Biological Samples at Cryogenic Temperatures. *Proc. Natl. Acad. Sci. U. S. A.* **2010**, *107* (3), 1094–1099.
- (18) Meitzner, G.; Gardea-Torresdey, J.; Parsons, J.; Scott, S. L.; Deguns, E. W. The Effect of Cryogenic Sample Cooling on X-Ray Absorption Spectra. *Microchem. J.* **2005**, *81* (1), 61–68.
- (19) Wakamiya, A.; Endo, M.; Sasamori, T.; Tokitoh, N.; Ogomi, Y.; Hayase, S.; Murata, Y. Reproducible Fabrication of Efficient Perovskite-Based Solar Cells: X-Ray Crystallographic Studies on the Formation of  $\text{CH}_3\text{NH}_3\text{PbI}_3$  Layers. *Chem. Lett.* **2014**, *43* (5), 711–713.
- (20) Ankudinov, A. L.; Rehr, J. J. Relativistic Calculations of Spin-Dependent X-Ray-Absorption Spectra. *Phys. Rev. B: Condens. Matter Mater. Phys.* **1997**, *56* (4), R1712–R1716.
- (21) Persson, I.; Lyczko, K.; Lundberg, D.; Eriksson, L.; Placzek, A. Coordination Chemistry Study of Hydrated and Solvated Lead(II) Ions in Solution and Solid State. *Inorg. Chem.* **2011**, *50* (3), 1058–1072.
- (22) Hao, F.; Stoumpos, C. C.; Liu, Z.; Chang, R. P. H.; Kanatzidis, M. G. Controllable Perovskite Crystallization at a Gas–Solid Interface for Hole Conductor-Free Solar Cells with Steady Power Conversion Efficiency over 10%. *J. Am. Chem. Soc.* **2014**, *136* (46), 16411–16419.
- (23) Guo, Y.; Shoyama, K.; Sato, W.; Matsuo, Y.; Inoue, K.; Harano, K.; Liu, C.; Tanaka, H.; Nakamura, E. Chemical Pathways Connecting Lead(II) Iodide and Perovskite via Polymeric Plumbate(II) Fiber. *J. Am. Chem. Soc.* **2015**, *137* (50), 15907–15914.
- (24) Downward, L.; Booth, C. H.; Lukens, W. W.; Bridges, F. A Variation of the F-Test for Determining Statistical Relevance of Particular Parameters in EXAFS Fits. In *AIP Conference Proceedings*; AIP Publishing: Melville, NY, 2007; Vol. 882, pp 129–131.
- (25) McLeod, J. A.; Wu, Z.; Sun, B.; Liu, L. The Influence of the I/Cl Ratio on the Performance of  $\text{CH}_3\text{NH}_3\text{PbI}_3\text{-xCl}_x$ -Based Solar Cells: Why Is  $\text{CH}_3\text{NH}_3\text{I:PbCl}_2 = 3:1$  the “magic” Ratio? *Nanoscale* **2016**, *8*, 6361–6368.
- (26) Manser, J. S.; Reid, B.; Kamat, P. V. Evolution of Organic–Inorganic Lead Halide Perovskite from Solid-State Iodoplumbate Complexes. *J. Phys. Chem. C* **2015**, *119* (30), 17065–17073.
- (27) Huang, F.; Dkhissi, Y.; Huang, W.; Xiao, M.; Benesperi, I.; Rubanov, S.; Zhu, Y.; Lin, X.; Jiang, L.; Zhou, Y.; et al. Gas-Assisted Preparation of Lead Iodide Perovskite Films Consisting of a Monolayer of Single Crystalline Grains for High Efficiency Planar Solar Cells. *Nano Energy* **2014**, *10*, 10–18.
- (28) Deng, Y.; Peng, E.; Shao, Y.; Xiao, Z.; Dong, Q.; Huang, J. Scalable Fabrication of Efficient Organolead Trihalide Perovskite Solar Cells with Doctor-Bladed Active Layers. *Energy Environ. Sci.* **2015**, *8* (5), 1544–1550.
- (29) Xiao, M.; Huang, F.; Huang, W.; Dkhissi, Y.; Zhu, Y.; Etheridge, J.; Gray-Weale, A.; Bach, U.; Cheng, Y.-B.; Spiccia, L. A Fast Deposition-Crystallization Procedure for Highly Efficient Lead Iodide Perovskite Thin-Film Solar Cells. *Angew. Chem.* **2014**, *126* (37), 10056–10061.
- (30) Ostwald, W. Studien Über Die Bildung Und Umwandlung Fester Körper. 1. Abhandlung: Übersättigung Und Überkaltung. *Z. Phys. Chem.* **1897**, *22*, 289–330.
- (31) Tidhar, Y.; Edri, E.; Weissman, H.; Zohar, D.; Hodes, G.; Cahen, D.; Rybtchinski, B.; Kirmayer, S. Crystallization of Methyl Ammonium Lead Halide Perovskites: Implications for Photovoltaic Applications. *J. Am. Chem. Soc.* **2014**, *136* (38), 13249–13256.
- (32) Soe, C. M. M.; Stoumpos, C. C.; Harutyunyan, B.; Manley, E. F.; Chen, L. X.; Bedzyk, M. J.; Marks, T. J.; Kanatzidis, M. G. Room Temperature Phase Transition in Methylammonium Lead Iodide Perovskite Thin Films Induced by Hydrohalic Acid Additives. *ChemSusChem* **2016**, *9* (18), 2656–2665.
- (33) Li, G.; Zhang, T.; Zhao, Y. Hydrochloric Acid Accelerated Formation of Planar  $\text{CH}_3\text{NH}_3\text{PbI}_3$  Perovskite with High Humidity Tolerance. *J. Mater. Chem. A* **2015**, *3* (39), 19674–19678.
- (34) Chueh, C.-C.; Liao, C.-Y.; Zuo, F.; Williams, S. T.; Liang, P.-W.; Jen, A. K.-Y. The Roles of Alkyl Halide Additives in Enhancing Perovskite Solar Cell Performance. *J. Mater. Chem. A* **2015**, *3*, 9058–9062.
- (35) Zuo, C.; Ding, L. An 80.11% FF Record Achieved for Perovskite Solar Cells by Using the  $\text{NH}_4\text{Cl}$  Additive. *Nanoscale* **2014**, *6* (17), 9935–9938.
- (36) Yoon, S. J.; Stampelcoskie, K. G.; Kamat, P. V. How Lead Halide Complex Chemistry Dictates the Composition of Mixed Halide Perovskites. *J. Phys. Chem. Lett.* **2016**, *7* (7), 1368–1373.
- (37) Hambsch, M.; Lin, Q.; Armin, A.; Burn, P. L.; Meredith, P. Efficient, Monolithic Large Area Organohalide Perovskite Solar Cells. *J. Mater. Chem. A* **2016**, *4* (36), 13830–13836.
- (38) Qiu, W.; Merckx, T.; Jaysankar, M.; Masse de la Huerta, C.; Rakocevic, L.; Zhang, W.; Paetzold, U. W.; Gehlhaar, R.; Froyen, L.; Poortmans, J.; et al. Pinhole-Free Perovskite Films for Efficient Solar Modules. *Energy Environ. Sci.* **2016**, *9* (2), 484–489.